

Rossby Wave Instability in Accretion Discs with Large-Scale Poloidal Magnetic Fields

Cong Yu^{1,2,3*}, and Dong Lai²

¹ *Yunnan Astronomical Observatory, Chinese Academy of Sciences, Kunming, China*

² *Department of Astronomy, Cornell University, Ithaca, NY 14853, USA*

³ *Key Laboratory for the Structure and Evolution of Celestial Objects, Chinese Academy of Sciences, Kunming, 650011, China*

27 March 2022

ABSTRACT

We study the effect of large-scale magnetic fields on the non-axisymmetric Rossby wave instability (RWI) in accretion discs. The instability develops around a density bump, which is likely present in the transition region between the active zone and dead zone of protoplanetary discs. Previous works suggest that the vortices resulting from the RWI may facilitate planetesimal formation and angular momentum transport. We consider discs threaded by a large-scale poloidal magnetic field, with a radial field component at the disc surface. Such field configurations may lead to the production of magnetic winds or jets. In general, the magnetic field can affect the RWI even when it is sub-thermal (plasma $\beta \sim 10$). For infinitely thin discs, the instability can be enhanced by about 10 percent. For discs with finite thickness, with a radial gradient of the magnetic field strength, the RWI growth rate can increase significantly (by a factor of ~ 2) as the field approaches equipartition ($\beta \sim 1$). Our result suggests that the RWI can continue to operate in discs that produce magnetic winds.

Key words: accretion, accretion discs - hydrodynamics - waves - planet formation - magnetic field

1 INTRODUCTION

Radial density structures can be common in astrophysical discs. For instance, in proto-planetary discs, different degrees of coupling of magnetic field with disc gas could lead to a transition region where the disc material piles up (e.g., Gammie 1996; Matsumura & Pudritz 2003; Terquem 2008). Proto-planets can also induce dips/gaps in the disc through tidal interaction (Lin & Papaloizou 1986; Ward 1997). In accretion discs around black holes or neutron stars, sharp density contrasts can be created near inner disc edge inside which the disc gas plunges inwards (e.g. Lovelace et al. 2009).

Such density structures lead to shear flows that are susceptible to Kelvin-Helmholtz instability (Papaloizou & Pringle 1985; Papaloizou & Lin 1989; Lithwick 2009). A specific realization of this instability is the so-called Rossby Wave Instability (RWI) (Lovelace et al. 1999; Li et al. 2000,2001). For two-dimensional (vertically integrated) barotropic discs, the RWI relies on the existence of an extremum in the background fluid vortensity (also called potential vorticity; see Drazin & Reid 2004; Narayan et al. 1987), defined by $\zeta = \kappa^2/(2\Omega\Sigma)$, where Σ is the disc

surface density, Ω the disc rotation rate and $\kappa^2 = 4\Omega^2 + 2r\Omega d\Omega/dr$ is the square of the radial epicyclic frequency. Since Rossby waves propagate along the gradient of vortensity, the instability can be understood as arising from the interaction between two Rossby waves propagating on each side of the vortensity extremum (e.g., Tagger 2001; Lai & Tsang 2009).

The nonlinear development of the RWI in discs leads to the production of vortices, which can accelerate the growth of meter-sized solids by concentrating dust grains and thus enhance the formation of planetesimals (Barge & Sommeria 1995; Johansen et al. 2004; Varniere & Tagger 2006; Heng & Kenyon 2010). Such vortices may also induce sizable angular momentum transfer in the radial direction (Li et al. 2001). The vortices formed at the edge of planetary gaps can affect the rate of planet migration (de Val-Borro et al. 2007; Yu et al. 2010; Lin & Papaloizou 2011a,b).

While most studies of the RWI deal with two-dimensional (height-integrated) discs, Meheut et al. (2010,2012) carried out the global simulations of the RWI in 3D discs [see also Lyra & Mac Low (2012) for MHD simulations of 3D discs with no vertical stratification]. They showed that the Rossby vortices have significant vertical structure, which affects the long-term evolution of the vortices. Meheut, Yu & Lai (2012) and Lin (2012)

* Email: cyu@ynao.ac.cn

studied the linear RWI in 3D vertically stratified discs, showing that while the RWI is basically a 2D instability, appreciable vertical velocities can be induced in the disc.

Magnetic fields are present in most accretion discs and can greatly change the dynamics of discs. It is generally thought that turbulence induced by the magneto-rotational instability (MRI; Balbus & Hawley 1998) is responsible for angular momentum transport in ionized discs. Recent simulations including ambipolar diffusion, however, suggest that the MRI associated with small-scale magnetic field may not be adequate to account for the angular momentum transport in protoplanetary discs, even in the “active zone” (Bai & Stone 2011). On the other hand, large-scale poloidal magnetic fields threading the accretion disc can generate outflows/jets and play an important role in the angular momentum transport (e.g., Blandford & Payne 1982). Large-scale magnetic fields are naturally present in the early phase of star formation. They may be advected inward with the accretion flow (e.g., Lubow et al. 1994), building up significant strength in the disc. The large-scale magnetic field may also counteract the disk self-gravity effect, thereby influencing disc fragmentation (Lizano et al. 2010).

Recently, Yu & Li (2009) showed from linear analysis that a weak (sub-thermal) toroidal magnetic field in the disc can completely suppress the RWI. This suppression results from the modification by the magnetic field to the wave absorption at the corotation resonance (see Fu & Lai 2011). In this paper, we study the effects of large-scale poloidal magnetic fields on the RWI. As noted above, such a large-scale field is essential for producing bipolar outflows and may be necessary for angular momentum transport in the disc. Since the growth of the RWI is primarily due to in-disc motion (Meheut et al. 2012), we will focus on 2D disc dynamics in this paper. However, we will consider the effect of finite disc thickness on the RWI growth rate while neglecting vertical stratification.

Note that in our models (see Section 2), the large-scale poloidal magnetic field provides a coupling between the dynamics of the disc and the magnetosphere (assumed to be current-free). We consider perturbations that have no vertical structure *inside* the disc (i.e., the vertical wavenumber $k_z = 0$). Thus, we do not include MRI, which generally involves perturbations with finite k_z . Our basic disc-magnetosphere setup is self-consistent. Similar setups have been considered by various authors in different contexts (e.g., Spruit et al. 1995; Tagger & Pallet 1999; Lizano et al. 2010).

Our paper is organized as follows. In §2, the basic disc equations with large-scale magnetic fields are derived. In §3, we present the results of RWI of thin magnetized discs. In §4, we consider the effects of finite disc thickness. and we conclude in §5.

2 BASIC EQUATIONS

We consider a thin conducting disc threaded by a magnetic field. The height-integrated mass continuity equation and

momentum equation read

$$\frac{\partial \Sigma}{\partial t} + \nabla_{\perp} \cdot (\Sigma \mathbf{u}) = 0, \quad (1)$$

$$\frac{d\mathbf{u}}{dt} = -\frac{1}{\Sigma} \nabla_{\perp} P + \frac{1}{4\pi\Sigma} B_z [\mathbf{B}]_{-}^{+} + \mathbf{g}, \quad (2)$$

where ∇_{\perp} is 2D operator (acting on the disc plane), Σ , P and \mathbf{u} are the surface density, height-integrated pressure and height-averaged velocity, respectively, $\mathbf{g} = -g(r)\hat{r}$ (with $g = GM/r^2$) is the gravitational acceleration, $[\mathbf{B}]_{-}^{+} \equiv \mathbf{B}(z = H) - \mathbf{B}(z = -H)$ (with H the half-thickness of the disc), and we have used $[B^2]_{-}^{+} = 0$. In this section we are considering infinitely thin discs, i.e., in the limit $H/r \rightarrow 0$. As a result, we neglect the *internal* magnetic force acting on the disc in Equation (2). The effect of finite disc thickness will be considered in Section 4.

For an equilibrium disc, the unperturbed velocity is $\mathbf{u} = (0, r\Omega, 0)$ (in cylindrical coordinates), with the angular velocity determined by

$$-\Omega^2 r = -\frac{1}{\Sigma} \frac{dP}{dr} - g + \frac{B_z}{2\pi\Sigma} B_r^{+}, \quad (3)$$

where $B_r^{+} = B_r(z = H) = -B_r^{-}$. The unperturbed disc has $B_{\phi}^{+} = 0$. Note that B_r is nonzero only outside the discs, which has different signs just above and below the disc. Inside the disc, B_r is zero and the differential rotation of the disc will not lead to generation of B_{ϕ} inside the disc.

Note that the disc dynamics are coupled with the large scale poloidal magnetic field outside the disc, i.e., the disc magnetosphere. Now consider small-amplitude perturbations of the disc. Assuming that all perturbed quantities are proportional to $\exp(im\phi - i\omega t)$, where $m = 1, 2, \dots$ is the azimuthal wave number and ω is the complex frequency, then the linearized fluid perturbation equations read

$$-i\tilde{\omega} \delta\Sigma = -\nabla_{\perp} \cdot (\Sigma \delta\mathbf{u}), \quad (4)$$

$$-i\tilde{\omega} \delta u_r - 2\Omega \delta u_{\phi} = -\frac{\partial}{\partial r} \delta h + \frac{B_z}{2\pi\Sigma} \delta B_r^{+} + \frac{B_r^{+}}{2\pi} \delta \left(\frac{B_z}{\Sigma} \right), \quad (5)$$

$$-i\tilde{\omega} \delta u_{\phi} + \frac{\kappa^2}{2\Omega} \delta u_r = -\frac{im}{r} \delta h + \frac{B_z}{2\pi\Sigma} \delta B_{\phi}^{+}, \quad (6)$$

where $\tilde{\omega} = \omega - m\Omega$ is the Doppler-shifted frequency, κ is the radial epicyclic frequency, and $\delta h = \delta P/\Sigma$ is the enthalpy perturbation (we assume barotropic discs). The magnetic field induction equation in the disc reads

$$-i\tilde{\omega} \delta B_z = -\nabla_{\perp} \cdot (B_z \delta\mathbf{u}). \quad (7)$$

Combining Eqs. (4) and (7), we have

$$\delta \left(\frac{B_z}{\Sigma} \right) = -\xi_r \frac{d}{dr} \left(\frac{B_z}{\Sigma} \right), \quad (8)$$

where $\xi_r = \delta u_r / (-i\tilde{\omega})$ is the Lagrangian displacement. Equation (8) can also be derived from $(d/dt)(B_z/\Sigma) = 0$. In terms of ξ_r and δh , the magnetic field perturbation is

$$\delta B_z = D_1 \xi_r + D_2 \delta h, \quad (9)$$

with

$$D_1 = B_z \frac{d}{dr} \left(\ln \frac{\Sigma}{B_z} \right), \quad D_2 = \frac{B_z}{c_s^2}, \quad (10)$$

where c_s is the sound speed.

To determine δB_r^+ and δB_ϕ^+ , we assume that the magnetic field outside the disc is a potential field (e.g., Spruit et al. 1995; Tagger & Pallet 1999). This amounts to assuming that the Alfvén speed above and below the disc is sufficiently high that currents are dissipated quickly (on the disc dynamical timescale). Define the magnetic potential $\delta\Phi_M$ outside the disc via

$$\delta\mathbf{B} = -\text{sign}(z)\nabla\delta\Phi_M. \quad (11)$$

Then $\delta\Phi_M$ satisfies the Poisson equation (Tagger & Pallet 1999)

$$\nabla^2\delta\Phi_M = -2\delta B_z\delta(z), \quad (12)$$

where $\delta(z)$ is the Dirac delta function. The integral solution of (12) is

$$\delta\Phi_M(r) = \int \delta B_z(r') \left[\frac{\alpha}{2} b_{1/2}^m(\alpha) \right] dr', \quad (13)$$

where $\alpha = r'/r$, and the Laplace coefficient is defined by

$$b_s^m(\alpha) = \frac{2}{\pi} \int_0^\pi \frac{\cos m\phi}{(\alpha^2 + \epsilon_0^2 + 1 - 2\alpha\cos\phi)^s} d\phi, \quad (14)$$

with ϵ_0 the softening parameter (of order the dimensionless disk thickness H/r). The perturbed radial magnetic field at the upper disc surface is

$$\begin{aligned} \delta B_r^+ &= -\frac{d}{dr}\delta\Phi_M \\ &= \int \delta B_z(r') \left(\frac{\alpha}{2r} \right) \left[b_{1/2}^m(\alpha) + \alpha \frac{db_{1/2}^m(\alpha)}{d\alpha} \right] dr', \end{aligned} \quad (15)$$

and the azimuthal field is $\delta B_\phi^+ = -(im/r)\delta\Phi_M$.

In our numerical calculations, we use the variable ξ_r and δh . The corresponding perturbation equations are

$$\begin{aligned} \frac{d\xi_r}{dr} &= -\left(\frac{2m\Omega}{r\tilde{\omega}} + \frac{1}{r} + \frac{d\ln\Sigma}{dr} \right) \xi_r \\ &\quad - \left(\frac{1}{c_s^2} - \frac{m^2}{r^2\tilde{\omega}^2} \right) \delta h + \frac{m^2}{r^2\tilde{\omega}^2} \frac{B_z}{2\pi\Sigma} \delta\Phi_M, \end{aligned} \quad (16)$$

$$\begin{aligned} \frac{d}{dr}\delta h &= \left(\tilde{\omega}^2 - \kappa^2 + \frac{B_r^+}{2\pi\Sigma} D_1 \right) \xi_r + \frac{2m\Omega}{r\tilde{\omega}} \delta h \\ &\quad - \frac{B_z}{2\pi\Sigma} \frac{d\delta\Phi_M}{dr} + \frac{2m\Omega}{r\tilde{\omega}} \frac{B_z}{2\pi\Sigma} \delta\Phi_M. \end{aligned} \quad (17)$$

3 RESULTS FOR THIN DISCS

We consider a density bump in the disc of the form

$$\frac{\Sigma(r)}{\Sigma_0} = 1 + (A-1) \exp\left[-\frac{(r-r_0)^2}{2\Delta^2} \right]. \quad (18)$$

We adopt $A = 1.2$ and $\Delta = 0.05r_0$ throughout this paper. We further assume $c_s = 0.1r_0\Omega_0 = \text{constant}$.

In this section, B_z is taken as a constant independent of r (we will consider varying B_z in Sections 4-5). The magnitude of B_z is specified by the dimensionless ratio

$$\hat{B}_z = \frac{B_z}{(\Sigma_0\Omega_0^2 r_0)^{1/2}}, \quad (19)$$

where the subscript “0” implies that the quantities evaluated at $r = r_0$. The corresponding plasma β parameter in the disc at $r = r_0$ is

$$\beta = \frac{8\pi\rho c_s^2}{B_z^2} = \frac{4\pi H_0}{r_0} \hat{B}_z^{-2}, \quad (20)$$

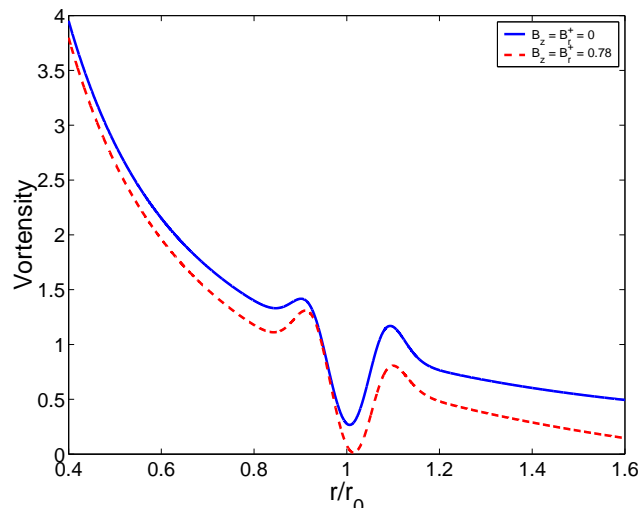


Figure 1. Vortensity profiles for magnetized discs with $\hat{B}_z = 0.78$, corresponding to the plasma $\beta \simeq 2$. The solid line is for the case of $B_r^+ = 0$ and the dashed line for $B_r^+ = B_z$.

where we have used $H = c_s/\Omega_K \simeq c_s/\Omega$. We solve for the equilibrium rotation profile using Eq. (3). In Fig. 1 we show two examples of the vortensity profiles for the $B_r^+ = 0$ and $B_r^+ = B_z$ cases. Note that when $B_r^+ = 0$, the vortensity profile is the same as a nonmagnetic disc. If $B_r^+ \neq 0$, when B_z increases, the epicyclic frequency approaches zero gradually at the minimum, as does the vortensity.

Since the eigenfrequency ω is in general complex, equations (16)-(17) are a pair of first-order differential equations with complex coefficients which are functions of r . We solve these equations using the relaxation method (Press et al. 1992), replacing the ODEs by finite-difference equations on a mesh of points covering the domain of interest (typically $0.4 < r/r_0 < 1.6$). According to Eqs. (9), (13), and (15), both the magnetic potential and its derivative can be expressed in terms of linear combination of ξ_r and δh . For numerical convenience, we calculate the terms in the square bracket in Eqs. (13) and (15) and store them for later use. Note that these terms are computed only once and can be used repetitively. The wave equations (16) and (17) can be cast in a matrix form that only deals with the variables $d\xi_r$ and dh . Standard relaxation scheme can be applied to the resulting matrix. We use uniform grid points in our calculations. The grid point number is typically chosen to be 350. We implement the radiative boundary conditions such that waves propagate away from the density structure in both the inner and outer parts of the disc (e.g., Yu & Li 2009). The relaxation method requires an initial trial solution that can be improved by the Newton–Raphson scheme. After iterations the initial trial solution converges to the eigenfunction of the the two-point boundary eigenvalue problem.

Figure 2 shows the growth rate of the RWI for different vertical magnetic field strengths of the disc. Real parts of the mode frequency for the solid line are all close to $\omega_r \simeq 0.99m\Omega_{K0}$. For the dashed line, real parts of the mode frequency decrease from $\omega_r \simeq 0.99m\Omega_{K0}$ to $\omega_r \simeq 0.95m\Omega_{K0}$ with the increase of magnetic field. Since B_z is assumed to be independent of r , the rotation profile of the disc is unaffected by B_z when $B_r^+ = 0$. In this case, we see that as B_z increases,

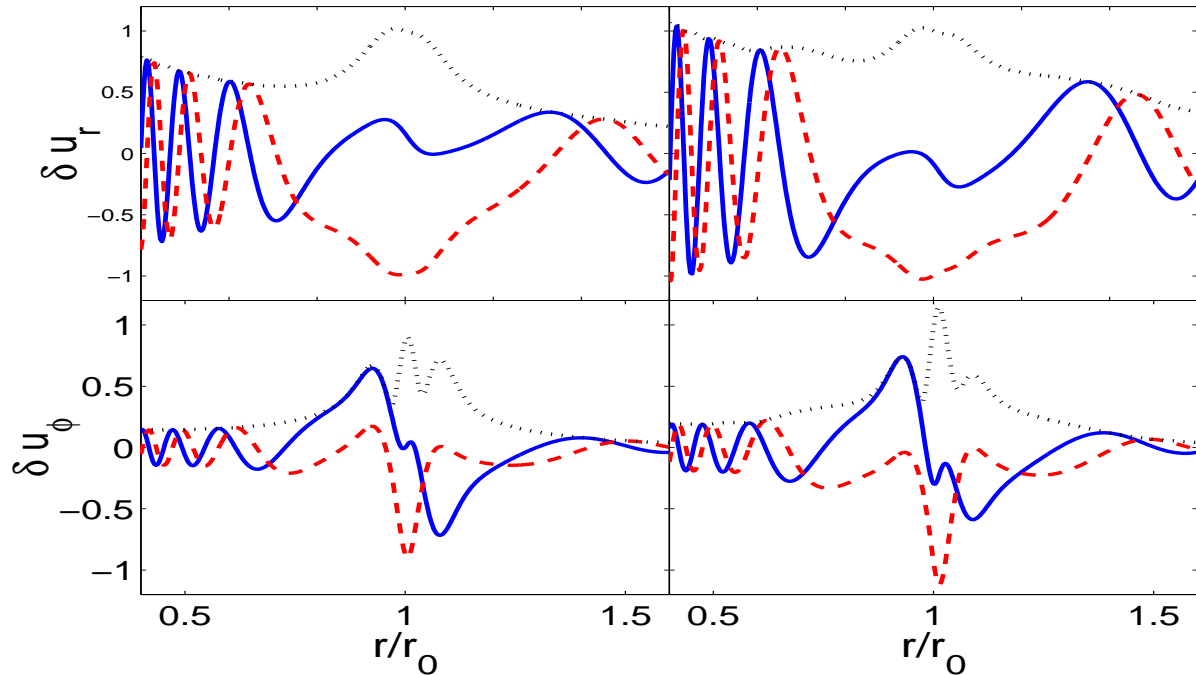


Figure 3. Eigenfunctions of the $m = 4$ the Rossby modes trapped near the density bump in the disc. The left panels show the non-magnetic case, and the right panels have $B_z = B_r^+ = 0.78$. The top panels show δu_r (the solid line is for the real part, the dashed line the imaginary part, and the dotted line the absolute value), and the bottom panels show δu_ϕ .

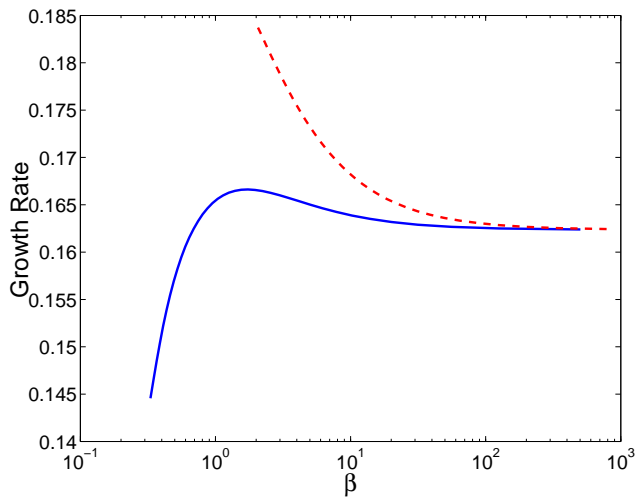


Figure 2. The growth rate (in units of Ω_{K0}) of the $m = 4$ RWI as a function of the plasma β parameter [with the corresponding vertical magnetic field strength B_z given by Eq. (20)]. The solid line is the case of $B_r^+ = 0$, and the dashed line $B_r^+ = B_z$.

the growth rate first increases slightly and then decreases. At $\beta \sim 0.3$, the growth rate is reduced by more than 10% compared to the $B_z = 0$ value. When $B_r^+ = B_z$, the equilibrium rotation profile of the disc is changed from the nonmagnetic disc. In this case, the growth rate increases monotonically with increasing B_z , reaching about 10% above the nonmagnetic value. Note that the dashed line terminates at $\beta \simeq 2$, since an even stronger magnetic field would make κ^2 negative. Comparing the two cases depicted in Fig. 2, it appears

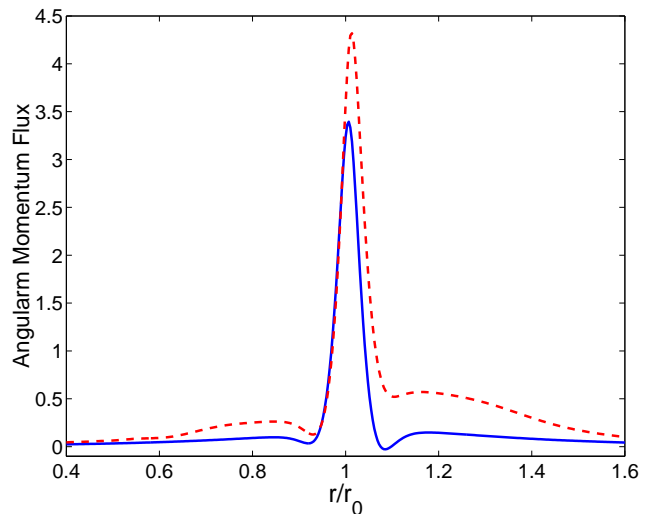


Figure 4. The angular momentum flux associated with the Rossby mode. The solid line is for the nonmagnetic case, and the dashed line for $\hat{B}_z = \hat{B}_r^+ = 0.78$. In both cases, the eigenfunction is normalized so that the maximum δu_r equals unity (near $r = r_0$). The higher angular momentum flux at $r \sim r_0$ for the magnetic case is consistent with the faster mode growth rate.

that the increase in the RWI growth rate mainly results from the deeper minimum of the disc equilibrium vortensity profile induced by the inclined ($B_r^+ > 0$) magnetic field.

Figure 3 gives some examples of the $m = 4$ eigenfunctions of Rossby modes trapped around the corotation radius, which is also close to the density bump. The left panels show the non-magnetized case, and the right panels show the

magnetized case with $B_r^+ = B_z = 0.78$. The amplitude of eigenfunctions are normalized so that the maximum absolute value of the radial velocity perturbation $|\delta u_r|$ equals unity (this maximum occurs at $r \simeq r_0$). The increase of δu_r near the inner boundary is due to the geometric effects (Meheut, Yu & Lai 2012). A Rossby mode excited around r_0 by the density bump can radiate into both the inner and outer parts of the disc as spiral density waves. The relative phase shift between the real and imaginary parts indicates this propagation.

To understand the origin of the enhanced RWI growth rate for magnetized discs, we show in Fig. 4 the angular momentum flux associated with the eigenmode for the non-magnetic disc and for the disc with $B_z = B_r^+ = 0.78$. The angular momentum flux $F(r)$ across a cylinder of radius r is given by (e.g., Goldreich & Tremaine 1979)

$$F(r) = \left\langle r^2 \int_0^{2\pi} \Sigma \delta u_r \delta u_\phi d\phi \right\rangle = \pi \Sigma r^2 \Re(\delta u_r \delta u_\phi^*) \quad (21)$$

where $\langle \rangle$ designates time average and the superscript * denotes complex conjugate. Note that waves carry negative (positive) angular momentum inside (outside) the corotation. The net positive (outward) angular momentum flux $F(r)$ around the corotation (close to the density bump) indicates the growth of the RWI. Higher angular momentum fluxes imply higher instability growth rates (see Fig. 4).

We have attempted a variational-principle analysis to determine the direct effect of magnetic force on the RWI (for a given vortensity profile). Such an analysis did not yield simple, unambiguous results, and therefore is not presented here. This is consistent with the non-monotonic behavior exhibited by the solid line in Fig. 2.

4 EFFECTS OF FINITE DISC THICKNESS

4.1 Model Equations

In Sections 2-3, we have adopted the infinitely thin disc approximation ($H/r \rightarrow 0$) and the "internal" disc magnetic force is neglected. When finite thickness of the disc is considered, an "internal" magnetic force term should be added to the right-hand side of Eq. (2):

$$\mathbf{f} = \frac{1}{\Sigma} \int dz \left[-\nabla_\perp \left(\frac{B^2}{8\pi} \right) + \frac{1}{4\pi} (\mathbf{B} \cdot \nabla_\perp) \mathbf{B} \right]. \quad (22)$$

Obviously, to include the 3D effect rigorously would require examining the vertical stratification of the density and magnetic field inside the disc – this is beyond the scope of this paper [see Meheut et al. (2012) and Lin (2012) for the case without magnetic field]. Here we consider a simple model where the internal density of the disc is assumed to be independent of z , so that

$$\Sigma = 2\rho H, \quad P = 2pH. \quad (23)$$

Then the internal magnetic force simplifies to

$$\mathbf{f} = \frac{1}{4\pi\rho} \left[-\nabla_\perp \left(\frac{B^2}{2} \right) + (\mathbf{B} \cdot \nabla_\perp) \mathbf{B} \right]. \quad (24)$$

We assume that only vertical field exists inside the unperturbed disc. The equilibrium rotational profile is then

determined by

$$-\Omega^2 r = -\frac{1}{\Sigma} \frac{dP}{dr} - g + \frac{B_z}{2\pi\Sigma} B_r^+ - \frac{B_z}{2\pi\Sigma} \left(H \frac{dB_z}{dr} \right). \quad (25)$$

To derive the modified perturbation equations including $\delta\mathbf{f}$, it is convenient to define a new perturbation variable $\delta\Pi$ in place of δh :

$$\delta\Pi \equiv \frac{\delta P}{\Sigma} + \frac{B_z \delta B_z}{4\pi\rho} = c_s^2 \frac{\delta\rho}{\rho} + \frac{B_z \delta B_z}{4\pi\rho}. \quad (26)$$

After some algebra, the final disc perturbation equations can be written in the following form:

$$\begin{aligned} \frac{d\xi_r}{dr} = & - \left(\frac{2m\Omega}{r\tilde{\omega}} + \frac{1}{r} + \frac{d\ln\Sigma}{dr} + D_4 \right) \xi_r \\ & + \left(\frac{m^2}{r^2\tilde{\omega}^2} - D_5 \right) \delta\Pi + \frac{m^2}{r^2\tilde{\omega}^2} \frac{B_z}{2\pi\Sigma} \delta\Phi_M, \end{aligned} \quad (27)$$

$$\begin{aligned} \frac{d}{dr} \delta\Pi = & \left(\tilde{\omega}^2 - \kappa^2 + \frac{B_r^+}{2\pi\Sigma} D_1 + D_6 \right) \xi_r \\ & + \left(\frac{2m\Omega}{r\tilde{\omega}} + D_7 - \frac{d\ln\rho}{dr} \right) \delta\Pi \\ & + \frac{2m\Omega}{r\tilde{\omega}} \frac{B_z}{2\pi\Sigma} \delta\Phi_M - \frac{B_z}{2\pi\Sigma} \frac{d\delta\Phi_M}{dr}, \end{aligned} \quad (28)$$

where

$$D_4 = \frac{-c_a^2}{c_s^2 + c_a^2} \frac{d}{dr} \left(\ln \frac{\Sigma}{B_z} \right), \quad c_a^2 = \frac{B_z^2}{4\pi\rho}, \quad (29)$$

$$D_5 = \frac{1}{c_s^2 + c_a^2}, \quad D_6 = \left[\frac{1}{\rho} \frac{d(p + \frac{1}{8\pi} B_z^2)}{dr} \right] D_4, \quad (30)$$

$$D_7 = \left[\frac{1}{\rho} \frac{d(p + \frac{1}{8\pi} B_z^2)}{dr} \right] D_5. \quad (31)$$

4.2 Results

Finite disc thickness has two effects on the RWI: one is the change in the equilibrium rotation profile and the other is the direct effect of $\delta\mathbf{f}$. We first examine the second effect by considering the case of constant B_z (no dependence of r). Figure 5 shows the result. We find that for the parameter considered ($c_s = 0.1$, or $H/r = 0.1$), the RWI growth rate is only slightly decreased (by less than 5%) compared to the $H/r \rightarrow 0$ limit.

Now consider the effect of the magnetic field gradient. With finite disc thickness, such a gradient modifies the equilibrium rotation profile. We use the following B_z profile:

$$B_z = B_{\text{mean}} + B_{\text{amp}} \tanh \left(\frac{r - r_0}{\Delta} \right). \quad (32)$$

Thus, the vertical magnetic field changes from $B_{\text{mean}} - B_{\text{amp}}$ at $(r - r_0)/\Delta \ll -1$ to $B_{\text{mean}} + B_{\text{amp}}$ at $(r - r_0)/\Delta \gg 1$. The length scale of the B_z variation is the same as the size of the density bump. The plasma β defined in Eq. (20) is evaluated at $r = r_0$ (where $B_z = B_{\text{mean}}$). We assume $B_{r+} = B_z$. Figure 6 shows some examples of the vortensity profiles. The blue curve is for the non-magnetized case, the dashed line is for the magnetized case where $B_{\text{mean}} = 0.64$, $B_{\text{amp}} = -0.6B_{\text{mean}}$. The magnetic field gradient in Eq. (25) alters the vortensity profile dramatically. The dashed line profile corresponds to the highest growth rate (dotted line, where $\beta \sim 3$) in Fig. 5.

The dotted line of Figure 5 shows the RWI growth rate

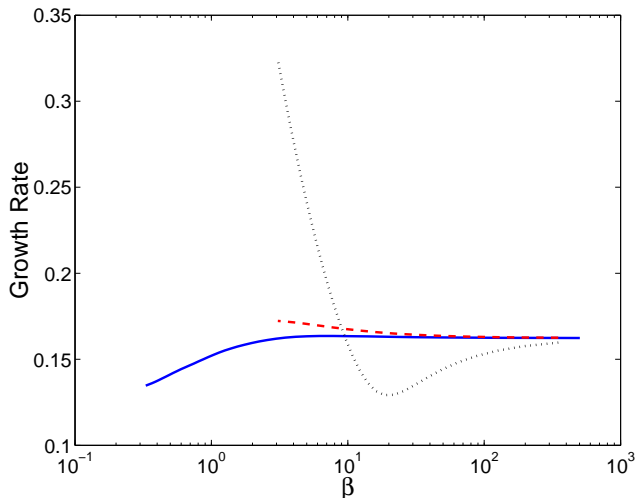


Figure 5. Growth rate of the $m = 4$ RWI as a function of the plasma β parameter for discs with finite thickness. The solid line is for the case of constant B_z with $B_r^+ = 0$, while the dashed line is for the case of constant $B_r^+ = B_z$. Note that in these two cases, the growth rates are very close to the cases depicted in Fig. 2 (where the internal magnetic force δf is neglected). The dotted line shows the case where $B_z(r)$ is given by Eq. (32) with $B_{\text{amp}} = -0.6B_{\text{mean}}$ and $B_r^+ = B_z$. As B_{mean} increases (or β decreases), the growth rate first decreases and then increases.

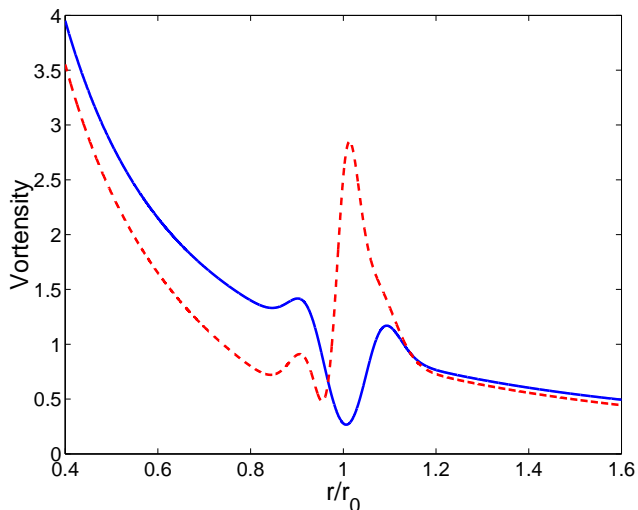


Figure 6. Vortensity in both non-magnetized (blue curve) and strongly magnetized (red curve, $B_{\text{mean}} = 0.64$, $B_{\text{amp}} = -0.6B_{\text{mean}}$) situations are shown. The magnetic field gradient change the vortensity profile significantly.

as a function of β in the case of $B_{\text{amp}} = -0.6B_{\text{mean}}$. We see that the growth rate depends on β in a non-monotonic way: As β decreases (B_{mean} increases), the growth rate first decreases, and then increases, reaching a factor of two compared to the non-magnetic value (e.g., at $\beta \simeq 3$, corresponding to the vortensity profile depicted by the dashed line of Fig. 6, the mode frequency is $\omega_r = 1.02m\Omega_{K0}$ with $m = 4$, and the growth rate is $\omega_i = 0.32\Omega_{K0}$).

Figure 7 and Figure 8 illustrate how the RWI growth rate depends on the B_z gradient, for two different values of

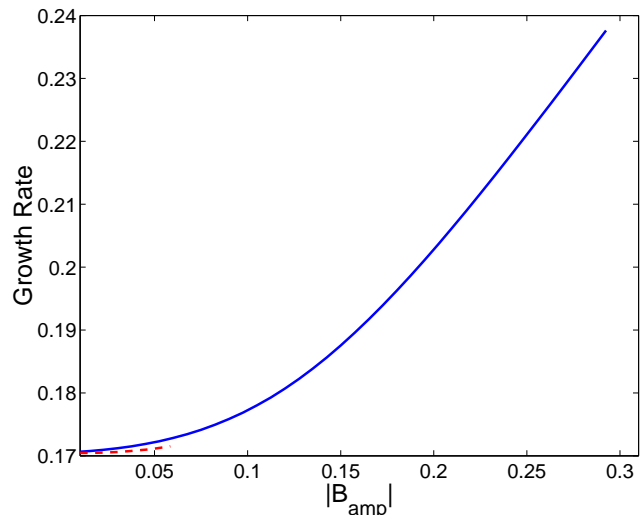


Figure 7. The dependence of the growth rate of the $m = 4$ RWI on on the B_z gradient. The B_z profile is given by Eq. (32), with $B_{\text{mean}} = 0.5$ (corresponding to $\beta = 5$) and $B_r^+ = B_z$. The solid line is for $B_{\text{amp}} < 0$ while the dashed line for $B_{\text{amp}} > 0$. In such a strong magnetic field regime, the magnetic field gradient (regardless of its sign) increases the instability growth rate. Note that the lines terminate at the point where the equilibrium rotation profile has $\kappa^2 = 0$ at some radius near the density bump.

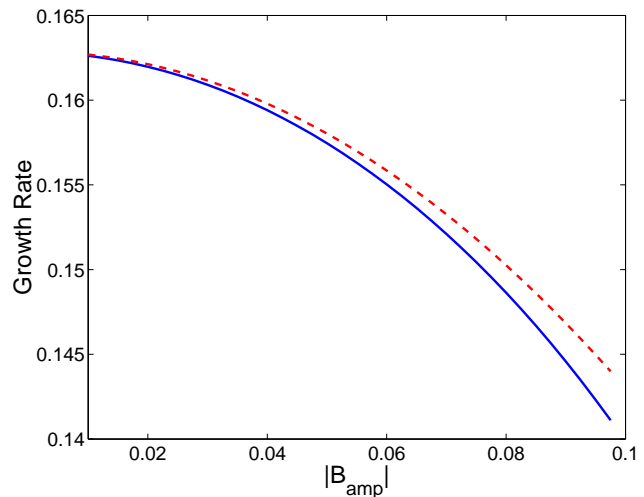


Figure 8. Same as Fig. 7 except for $B_{\text{mean}} = 0.1$ (corresponding to $\beta \sim 120$). In such a weak magnetic field regime, the growth rate of the RWI tends to be reduced by the magnetic field gradient.

B_{mean} . For small B_{mean} , the growth rate is reduced by the B_z gradient (regardless of the sign of the gradient); for larger B_{mean} , the growth rate is enhanced by the B_z gradient.

5 DISCUSSION AND CONCLUSION

In this paper we have carried out linear analysis of the Rossby wave instability (RWI) in accretion discs threaded by large-scale magnetic fields. The instability can develop around the extremum of disc vortensity [$\zeta = \kappa^2/(2\Omega\Sigma)$, vorticity divided by surface density], and may play an important role in planetesimal formation and angular momen-

tum transport in proto-planetary discs, and may also generate variabilities in black-hole accretion discs. Our results show that the large-scale magnetic field can affect (increase or decrease, depending on the field configuration) the RWI growth rate even when it has a sub-thermal strength (plasma $\beta \sim 10$ in the disc). For thin discs, the instability growth rate can be enhanced by the magnetic field by up to 10%. We have also considered discs with finite thickness (but ignoring vertical stratification), and shown that the RWI growth rate can be further increased (by a factor of ~ 2 when $\beta \sim 1$) with a steep radial gradient in the magnetic field strength. Just like the density bump, such field gradient may be present around the transition region between the active and dead zones in proto-planetary discs.

In general, the large-scale magnetic field influences the RWI in two ways, either through the direct effect of magnetic force on the perturbed fluid, or by modifying the equilibrium disc vortensity profile. We find that the first effect is typically smaller than the second.

Previous studies have shown that an ordered toroidal magnetic field *inside* the disc can suppress the RWI, even when the field strength is sub-thermal (Yu & Li 2009). This comes about because the in-disc toroidal field changes the behavior of wave absorption at the corotation resonance (see Fu & Lai 2011). By contrast, the large-scale poloidal field considered in this paper does not qualitatively affect the corotation resonance, and in most cases leads to an enhanced RWI. Our calculations of discs with finite thickness showed that the magnetic field gradient in the radial direction can significantly affect the dynamics of RWI. More rigorous treatments, taking into account the vertical stratification of the disc and including both poloidal and toroidal magnetic field, would be useful.

The magnetic field - disc configurations studied in this paper are susceptible to the production of magneto-centrifugal winds. Recent works suggested that in proto-planetary discs, MRI-induced turbulence may be inadequate for transporting angular momentum and magnetic winds may be necessary (Bai & Stone 2011). Our result in this paper implies that the RWI can operate under the wind-producing conditions, potentially contributing to angular momentum transport in the disc.

ACKNOWLEDGMENTS

This work has been supported in part by NSF grant AST-1008245, NASA grants NNX12AF85G and NNX10AP19G. C. Y. thanks the support from National Natural Science Foundation of China (Grants 10703012, 11173057 and 11033008) and Western Light Young Scholar Program of CAS. Part of the computation is performed at HPC Center, Kunming Institute of Botany, CAS, China.

REFERENCES

Bai X. N. & Stone J. M., 2011, *ApJ*, 736, 144
 Balbus S. A., & Hawley J. F., 1998, *Rev. Mod. Phys.*, 70, 1
 Barge P., & Sommeria J., 1995, *A&A*, 295, 1
 Blandford, R. D., & Payne, D. G. 1982, *MNRAS*, 199, 883

de Val-Borro M., et al., 2007, *A&A*, 471, 1043
 Drazin, P.G., & Reid, W. H. 2004, *Hydrodynamic Stability* (2nd ed.; Cambridge: Cambridge Univ. Press)
 Fu W., & Lai D., 2011, *MNRAS*, 410, 399
 Gammie C. F., 1996, *ApJ*, 457, 355
 Goldreich, P., & Tremaine, S. 1979, *ApJ*, 233, 857
 Heng K., & Kenyon, S. J., 2010, *MNRAS*, 408, 1476
 Johansen A., Andersen A. C., & Brandenburg A., 2004, *A&A*, 417, 361
 Lai D., & Tsang D., 2009, *MNRAS*, 393, 979
 Lin D. N. C., & Papaloizou J. C. B., 1986, *ApJ*, 309, 846
 Li H., et al., 2001, *ApJ*, 551, 874
 Li H., et al., 2000, *ApJ*, 503, 1023
 Lin M. K., arXiv:1203.2630
 Lin M. K., & Papaloizou J. C. B., 2011a, *MNRAS*, 415, 1426
 Lin M. K., & Papaloizou J. C. B., 2011b, *MNRAS*, 415, 1445
 Lithwick Y., 2009, *ApJ*, 693, 85
 Lizano S., et al., 2010, *ApJ*, 724, 1561
 Lovelace R.V.E., et al., 1999, *ApJ*, 513, 815
 Lovelace R.V.E., Turner L., & Romanova M.M. 2009, *ApJ*, 701, 225
 Lubow, S. H., Papaloizou, J. C. B., & Pringle J. E. 1994, *MNRAS*, 267, 235
 Lyra W., & Mac Low M., arXiv:1204.5711
 Matsumura, S., Pudritz, R.E. 2003, *ApJ*, 598, 645
 Meheut H., et al., 2010, *A&A*, 516, 31
 Meheut, H., et al., 2012, *A&A*, 542, 9
 Meheut H., Yu C., & Lai D., 2012, *MNRAS*, 422, 2399
 Narayan R., Goldreich P., & Goodman J., 1987, *MNRAS*, 228, 1
 Papaloizou J. C. B., & Lin, D. N. C. 1989, *ApJ*, 344, 645
 Papaloizou J. C. B., & Pringle J. E., 1985, *MNRAS*, 213, 799
 Press W. H., Teukolsky S. A., Vetterling W. T., Flannery B. P., 1992, *Numerical Recipes in FORTRAN*. Cambridge Univ. Press, Cambridge
 Spruit H. C., Stehle R., & Papaloizou J. C. B., 1995, *MNRAS*, 275, 1223
 Tagger, M. 2001, *A&A*, 380, 750
 Tagger M., & Pellet R., 1999, *A&A*, 349, 1003
 Tequerm, C. E. J. M. L. J., 2008, *ApJ*, 689, 532
 Varnière P. & Tagger M., 2006, *A&A*, 446, 13
 Ward, W. R., 1997, *Icarus*, 126, 261
 Yu C., & Li H., 2009, *ApJ*, 702, 75
 Yu C., et al., 2010, *ApJ*, 712, 198